

LATR: 3D Lane Detection from Monocular Images with Transformer

Yueru Luo^{1,2} Chaoda Zheng^{1,2} Xu Yan^{1,2} Tang Kun³ Chao Zheng³
 Shuguang Cui^{2,1} Zhen Li^{2,1*}
¹ FNii, CUHK-Shenzhen ² SSE, CUHK-Shenzhen ³ Tencent Map, T Lab

Abstract

3D lane detection from monocular images is a fundamental yet challenging task in autonomous driving. Recent advances primarily rely on structural 3D surrogates (e.g., bird’s eye view) that are built from front-view image features and camera parameters. However, the depth ambiguity in monocular images inevitably causes misalignment between the constructed surrogate feature map and the original image, posing a great challenge for accurate lane detection. To address the above issue, we present a novel **LATR** model, an end-to-end 3D lane detector that uses 3D-aware front-view features without transformed view representation. Specifically, **LATR** detects 3D lanes via cross-attention based on query and key-value pairs, constructed using our lane-aware query generator and dynamic 3D ground positional embedding. On the one hand, each query is generated based on 2D lane-aware features and adopts a hybrid embedding to enhance the lane information. On the other hand, 3D space information is injected as positional embedding from an iteratively-updated 3D ground plane. **LATR** outperforms previous state-of-the-art methods on both synthetic Apollo and realistic OpenLane by large margins (e.g., **11.4** gains in terms of F1 score on OpenLane). Code will be released at <https://github.com/JMoonr/LATR>.

1. Introduction

3D Lane Detection is critical for various applications in autonomous driving, such as trajectory planning and lane keeping [46]. Despite the remarkable progress of LiDAR-based methods in other 3D perception tasks [54, 13], recent advances in 3D lane detection prefer using a monocular camera since it owns desirable advantages compared to LiDARs. Apart from the low deployment cost, cameras offer a more extended perception range compared to other sensors and can produce high-resolution images with rich textures, which are crucial for detecting slim and long-span lanes.

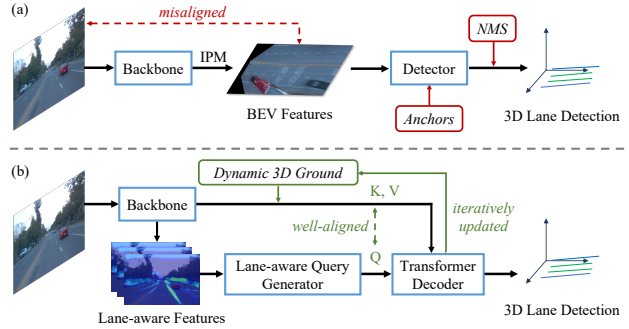


Figure 1. (a) Previous methods mainly utilize camera parameters and inverse perspective mapping (IPM) to transform the features into a surrogate space (e.g., BEV), and further perform 3D lane detection through anchors and non-maximum suppression (NMS). (b) We propose the novel **LATR**, an anchor-free, and NMS-free Transformer architecture, to perform 3D lane detection right on the front view. Using lane-aware queries and dynamic 3D ground positional embedding, our model produces well-aligned 3D features and achieves superior 3D lane detection.

Due to the lack of depth information, detecting 3D lanes from monocular images is challenging. A straightforward solution is to reconstruct the 3D lane layout based on 2D segmentation results and per-pixel depth estimation, as proposed in SALAD [47]. However, this method requires high-quality depth data for training and heavily relies on the precision of the estimated depth. Alternatively, CurveFormer [1] employs polynomials to model the 3D lane from the front view. While it avoids indefinite view transformation, the polynomial form adopted in their design restricts the flexibility of diverse lane shapes. By contrast, current mainstream methods favor the utilization of 3D surrogate representations [7, 5, 8, 23, 3, 14]. These surrogate representations are constructed based on front-view image features and camera parameters, with no reliance on depth information. Since lanes inherently reside on the road, most of these methods build the 3D surrogate by projecting the image features into a bird’s eye view (BEV) via inverse perspective mapping (IPM). However, the IPM is strictly based on the flat ground assumption, thereby introducing misalignment between the 3D surrogate and the original image in many real driving scenarios (e.g., uphill/downhill and

*Corresponding author

bumps). This misalignment, entangled with distortions, inevitably hinders the accurate estimation of the road structure and endangers driving safety. Despite attempts [3] made to relieve this issue by updating the BEV surrogate via deformable attention [55], the problem of misalignment remains unavoidable.

Based on the above observation, we aim to improve 3D lane detection by *directly locating 3D lanes right from the front view without any intermediate 3D surrogate through lane-aware queries*. Inspired by the 2D object detector DETR [2], we streamline lane detection as an end-to-end set prediction problem, forming **L**ane detection **T**Ransformer (**LATR**). LATR detects 3D lanes from the front view image using *lane-aware queries* and *dynamic 3D ground positional embedding*. We devise a lane representation scheme to describe lane queries, better capturing the property of 3D lanes. Additionally, we leverage lane-aware features to offer queries rich semantic and spatial prior. Since pure front-view features lack awareness of the 3D space, we inject the 3D positional information from a hypothetical 3D ground into the front-view features. This hypothetical ground initialized as a horizontal grid, is iteratively optimized to fit the ground truth road. Finally, the lane-aware queries interact with the 3D-aware features through a transformer decoder, followed by MLPs to produce 3D lane predictions.

Our main contributions are the following:

- We propose **LATR**, an end-to-end 3D lane detection framework based on Transformer. By directly detecting 3D lanes from the front views, without using any 3D surrogate representations, LATR offers efficiency and avoids feature misalignment present in prior methods.
- We introduce a lane-aware query generator that uses dynamically extracted lane-aware features to initialize query embeddings. Moreover, a dynamic positional embedding is proposed to bridge 3D space and 2D images, which derives from a constructed 3D ground that is iteratively updated under supervision.
- We conduct thorough experiments on the benchmark datasets of OpenLane, Apollo, and ONCE-3DLanes. Our proposed LATR outperforms previous SoTA methods by large margins (+11.4 improvement on OpenLane, +4.3 on Apollo, and +6.76 on ONCE-3DLanes *w.r.t.* F1 score).

2. Related Work

2.1. 2D Lane Detection

Benefiting from deep learning, 2D lane detection has made significant progress. Primary approaches formulate the problem in four manners. 1) *Segmentation-based* methods primarily resort to pixel-wise classification to generate lane masks [33, 32, 52], which are further post-processed to form a set of lanes through specific designs. 2) *Anchor-based* approaches mainly leverage line-like an-

chors to regress the offsets relative to targets [15, 41, 53]. Besides, row-based anchors are heuristically devised to classify row-wise pixels into lanes [49, 35, 20]. Further, to mitigate the detection error of side lanes, Qin *et al.* [36] extended the row-wise representation to a hybrid one, using row and column anchors. Eigenlanes [11] proposes to detect lanes in the eigenlane space, representing each lane as a linear combination of eigenlanes. 3) *Keypoint-based* approaches are proposed to more flexibly model lane positions [12, 37, 43, 11], which first estimated locations of points and then clustered into distinct lanes using different schemes. 4) *Curve-based* approaches attempt to fit the lane curve shape based on different curve representations, *e.g.*, polynomial curve [42], Bézier curve [6]. Despite these promising progresses in 2D lane detection, there is a non-negligible gap between the 2D results and the need in the real application scenario, *i.e.*, accurate 3D positions.

2.2. 3D Lane Detection

To acquire accurate 3D positions in realistic scenarios, 3D lane detection was proposed to encourage related studies. Compared to the 2D lane task, nonetheless, there are fewer studies to explore the model design. Prevalent methods [7, 5, 8, 23, 3, 14] attempt to transform the 2D features into a surrogate 3D space based on inverse perspective mapping (IPM), which is under flat road assumption. Nonetheless, this assumption is easily broken when encountering uphill/downhill, which is common in driving scenarios. Thus, the latent feature representation is entangled with unexpected distortion caused by road height variety, which impairs the model’s reliability and jeopardizes traffic safety.

To tackle this problem, SALAD [47] utilizes image segmentation based on the front view, the results of which are further processed as 3D lanes assisted by additional depth estimation. However, dense depth annotation is required during training, and the depth estimation capability becomes their performance bottleneck. GP [14] resorts to 3D lane reconstruction to achieve detection. To preserve the structure of 3D lanes, they explicitly impose geometric constraints of the intra-lane and inter-lane relationship under sophisticatedly designed supervision. M²-3Dlane [30], instead, introduces LiDAR data to facilitate the monocular 3D lane detection. By leveraging LiDAR point clouds, they lift the image features into 3D space and further fuse the multi-modal features in BEV space. A concurrent work CurveFormer [1] also formulates detection directly on the perspective image space under the end-to-end transformer paradigm, while it represents lanes in a parametric form and forces the model to implicitly learn 3D positions. Although polynomial formulation could provide a compact structure of lanes, it suffers from the sensitivity of parameters and lacks the flexibility to represent diverse lanes in realistic driving environments.

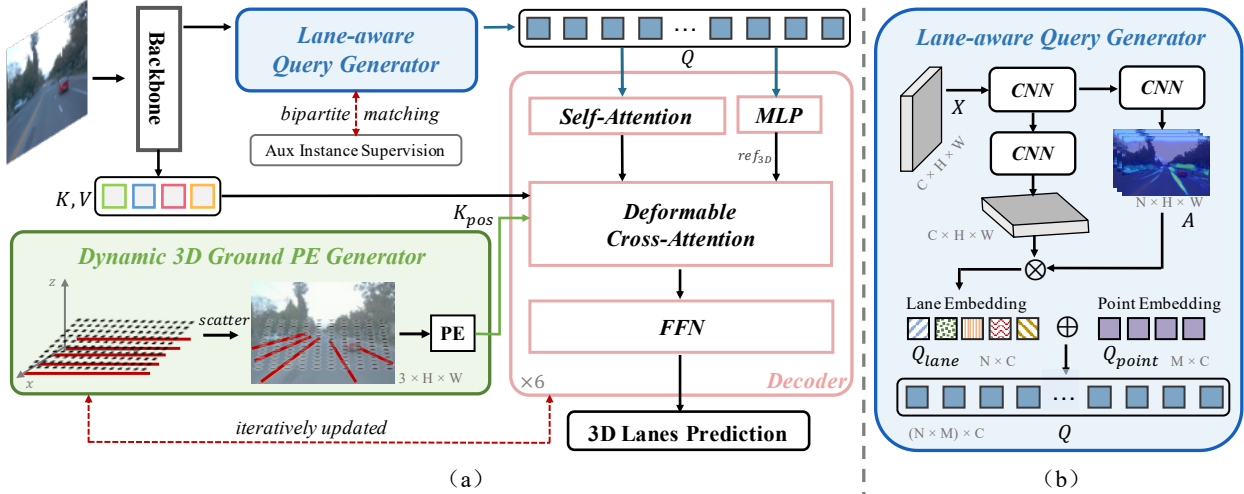


Figure 2. **The overall architecture.** LATR is a novel 3D lane detection framework that utilizes a Transformer-based approach, as shown in part (a). Specifically, the front-view image is first processed by the backbone network. Subsequently, a Lane-aware Query Generator generates queries that incorporate lane-level and point-level embeddings, as illustrated in (b). In addition, dynamic 3D ground positional embeddings are obtained through iterative refinement of a hypothetical 3D ground plane which is used to capture 3D information.

Different from previous works, LATR relies only on the front view and the monocular image to achieve end-to-end 3D lane detection, building the intra-lane and inter-lane geometric relationship without hard constraints [14]. Our queries are endowed with lane-aware information from a global perspective, which further integrates with dynamic 3D ground features to predict 3D lanes.

2.3. Object Detection with Transformers

DETR [2] is the pioneer that adopts the end-to-end Transformer architecture to object detection. Basically, DETR removes the need for heuristic designs in the previous CNN-based methods, *e.g.*, anchor box, NMS, and instead uses the learnable query to target the potential objects. Recently, there are a number of follow-up studies in camera-based object detection that adopt the end-to-end framework. To bridge 3D space and 2D image, monocular methods usually require depth estimation of either the entire image [10, 34], or foreground [51], or center of objects [29], while multi-view methods either require reconstruction [16, 17, 28] of dense 3D space or generate 3D frustums [25, 26].

Moreover, existing query-based object detection [2, 55, 16, 17, 28] perform query initialization either in a random manner, or by injecting tailored anchor design [45, 24] for 2D objects, or generating 3D frustum [25, 26] in the positional embeddings to provide localization information for 3D objects. Nonetheless, there are some limitations when directly applying these methods to 3D lane detection. First, the ambiguous learnable queries are hard to optimize [40] and take a toll on query features aggregation [45, 24]. Additionally, the learned queries hold fixed parameters, which limits the generalization. Second, due to the significant disparity between compact objects and slender lanes, those tai-

lored designs [45, 24] are not suitable (*e.g.*, anchor box-based query) or sub-optimal [50, 25] (*e.g.*, frustum in 3D space) for lane detection.

3. Method

Given an input image $\mathbf{I} \in \mathbb{R}^{3 \times H \times W}$, 3D lane detection aims to predict the 3D position of lanes within it. Lanes are represented by a collection of 3D points, denoted as $\mathbf{Y} = \{\mathbf{L}_i | i \in 1, \dots, N\}$, where N is the number of lanes in the image, and \mathbf{L}_i denotes the i -th lane. Each lane $\mathbf{L}_i = (\mathbf{P}_i, C_i)$ consists of a set of points $\mathbf{P}_i = \{(x_i^j, y_i^j, z_i^j)\}_{j=1}^M$ that construct the lane, where M is a predetermined cardinality of the output point set and C_i indicates the category. Normally, $y_i^{[*]}$ is set as a predefined longitudinal coordinate $\mathbf{Y}_{ref} = \{y_i^i\}_{i=1}^M$ [7, 8, 3].

3.1. Overall Architecture

The overall architecture of LATR is illustrated in Fig. 2. We first extract the feature map $\mathbf{X} \in \mathbb{R}^{C \times H \times W}$ from the input image using a 2D backbone. After that, we generate lane-aware queries $\mathbf{Q} \in \mathbb{R}^{(N \times M) \times C}$ using the Lane-aware Query Generator module, where N represents the number of lanes and each lane is depicted by M points. Note that $(N \times M)$ indicates flattened channels along corresponding dimensions. Subsequently, the lane-aware queries \mathbf{Q} aggressively interacting with the feature map \mathbf{X} via deformable attention [55]. Without constructing any misaligned 3D surrogate, we propose the Dynamic 3D Ground Positional Embedding (PE) Generator to enhance 2D features with 3D awareness during the deformable attention. Finally, we apply a prediction head on the updated queries to obtain the final lane prediction. Details of each component will be given in the following subsections.

3.2. Lane-aware Query Generator

Instead of adopting fixed learned features as queries in previous methods [2, 17, 25, 55], we propose a dynamic scheme to generate lane-aware query embeddings, which provide queries with valuable 2D lane priors based on image features. Moreover, to offer queries more flexibility in portraying lanes and implicitly modeling the relations of intra-lane and inter-lane, we represent the query embedding with diverse granularities, lane-level and point-level. The lane-level embedding captures the entire structure of each lane, while the point-level embedding gathers the local features located at $y^i \in \mathbf{Y}_{ref}$ as stated above. We then concert these two levels as our final query embeddings. This hybrid embedding scheme encodes queries with discriminative features of different lanes and enables each query to capture common patterns at a particular depth by sharing the same point-level embedding. The intuition here is that points located at the same depth across different lanes will be rescaled by the same factor when projected to the image. Meanwhile, being on the same road results in some shared properties among the lanes in 3D space, e.g., the same elevation. The inner structure of the proposed lane-aware query generator is presented in the right part of Fig. 2.

1) Lane-level embedding encodes features of N lane instances from the image feature map $\mathbf{X} \in \mathbb{R}^{C \times H \times W}$. Concretely, we utilize a lane-aware feature aggregator to gather features of distinct lanes, based on a set of instance activation maps (IAMs) $\mathbf{A} \in \mathbb{R}^{N \times (H \times W)}$ [4]. The IAMs are dynamically generated and can be formulated as:

$$\mathbf{A} = \sigma(\mathcal{F}([\mathbf{X}, \mathbf{S}])),$$

where \mathcal{F} is implemented by several convolution layers, σ is a sigmoid function, $[\cdot]$ denotes concatenation and \mathbf{S} is a two-channel feature map which represents the 2D spatial localization of pixels [22]. With IAMs, the lane-level embedding $\mathbf{Q}_{lane} \in \mathbb{R}^{N \times C}$ can be obtained via:

$$\mathbf{Q}_{lane} = \mathbf{A} \cdot \mathbf{X}^T.$$

During training, we add an auxiliary segmentation head [4] on top of \mathbf{Q}_{lane} to predict 2D lane instance masks, which are supervised by projected 3D annotations. Following [4], we assign ground-truth labels to N instance masks using dice-based bipartite matching. We also use the same matched results to assign labels to our final lane predictions. Please refer to our supplementary for more details.

2) Point-level embedding expresses how points relate to each other in a lane. Instead of deriving it from the image features, we represent it as a set of learnable weights $\mathbf{Q}_{point} \in \mathbb{R}^{M \times C}$, where each $Q_{point}^i \in \mathbb{R}^{1 \times C}$ corresponds to the embedding of a y^i in the predefined \mathbf{Y}_{ref} . These embeddings will be learned during training.

3) Lane-aware query embedding $\mathbf{Q} \in \mathbb{R}^{(N \times M) \times C}$ can be obtained using the following equation:

$$\mathbf{Q} = \mathbf{Q}_{lane} \oplus \mathbf{Q}_{point},$$

where \oplus denotes the broadcasting summation. The broadcast operation enables the model to distinguish different instances and group points based on lane-level embedding. Note that, sharing point-level embedding can help model relative relation and common features among points across different lanes without introducing geometric priors, e.g., point-distance constrain, and sophisticated supervision as done in previous methods [14].

3.3. Dynamic 3D Ground Positional Embedding

As discussed in Sec. 2.2, existing methods primarily either utilize a surrogate 3D space to estimate 3D lane positions [3, 8, 7, 5] or implicitly force the model to learn 3D positions [1]. Differently, we propose to use the prior that all lanes are located on the ground in the real world and construct a 3D plane to model the ground. Although there have been several attempts to leverage ground prior to facilitating 3D object detection, some make strong hypotheses like fixed ground [27], while others introduce extra prediction tasks, e.g., dense depth estimation [44, 38, 34], horizon line detection, and contact points detection [48]. However, predicting these extra tasks poses a significant challenge due to their high degree of freedom (DOF), and inaccurate predictions can inevitably undermine performance due to accumulative errors. In this paper, we tackle this problem by restricting the plane to only two DOF. Specifically, we encode the plane as the *key*'s positional embedding in each deformable attention module. As follows, we will delve into how to generate the *3D ground positional embedding* and update the hypothetical plane to dynamically approach the real ground with only 3D lane annotations.

Positional Embedding Generation. We first construct a 3D plane $\mathbf{P} \in \mathbb{R}^{P \times 3}$ represented by 3D grids with P points $\mathbf{P} = \{(x_i, y_i, z_i) | i \in 1, \dots, P\}$ and project all points into the 2D image using camera parameters T as:

$$d * [u, v, 1]^T = T \cdot [x, y, z, 1]^T. \quad (1)$$

We initialize the grid as a horizontal plane with z empirically set to -1.5 . Based on Eq. (1), we scatter all projected points into a 2D canvas $\mathbf{M}_p \in \mathbb{R}^{3 \times H \times W}$, which preserves 3D position for each projected point as:

$$\mathbf{M}_p[:, v, u] = (x, y, z), \quad (2)$$

where (u, v) and (x, y, z) denotes 2D and 3D coordinates defined in Eq. (1). For those pixels without projected points, we simply set them to 0s. Afterward, we obtain the 3D ground positional embedding $\mathbf{PE} \in \mathbb{R}^{C \times H \times W}$ via an MLP.

Dynamic Plane Update. In order to dynamically update the plane to approach the real ground, we predict a residual transformation matrix with two DOF (i.e., $\Delta\theta_x, \Delta z$) in each decoder layer, using image features and projected canvas,

$$[\Delta\theta_x, \Delta z] = \text{MLP}(\text{AvgPool}(\mathcal{G}([\mathbf{X}, \mathbf{M}_p]))) \quad (3)$$

where $[\cdot]$ represents concatenation, \mathcal{G} is two convolution

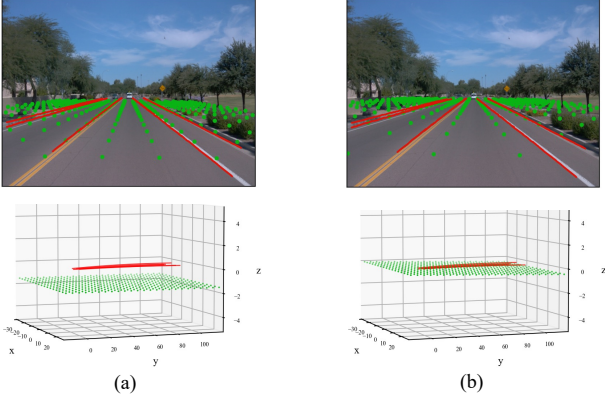


Figure 3. **An illustration of dynamic ground update.** Green points are sampled from our constructed 3D ground plane, and red lines represent ground truth lanes. (a) The left column demonstrates the initial 3D position of the constructed plane (green) and the ground truth (red). (b) The right column shows the updated position, where our constructed ground learned to find the real road position, *i.e.*, they are nearly in the same plane.

layers, \mathbf{X} denotes 2D features from backbone and \mathbf{M}_p is the projected canvas that encodes 3D positions from Eq. (2). Further, the transformation matrix can be formulated as:

$$D = \begin{bmatrix} 1 & 0 & 0 & 0 \\ 0 & \cos \Delta\theta_x & -\sin \Delta\theta_x & 0 \\ 0 & \sin \Delta\theta_x & \cos \Delta\theta_x & \Delta z \\ 0 & 0 & 0 & 1 \end{bmatrix}, \quad (4)$$

Then, we iteratively update the plane layer by layer via:

$$\tilde{\mathbf{P}}_l^\top = D \cdot \tilde{\mathbf{P}}_{l-1}^\top, \quad (5)$$

where $\tilde{\mathbf{P}}$ is the homogeneous representation of \mathbf{P} and l indexes the decoder layer. An algorithm is provided in our Supplementary to summarize the update procedure.

Supervision. To supervise the predicted transformation matrix D with two DOF, $\Delta\theta_x$, Δz . we project 3D lane annotations into images using camera parameters T , $l_{u,v} = T \cdot l_{x,y,z}$, where $l_{x,y,z}$ is 3D lane annotations and $l_{u,v}$ is the corresponding location on the 2D image. Similar to Eq. (2), we scatter all projected lanes into \mathbf{M}_l . Thus, we use projected 3D lane annotations to sparsely supervise the projected plane. Given \mathbb{P} , which represents the set of all pixels projected from the plane, and \mathbb{L} , the set of all projected 3D lane annotations, our loss can be formulated as:

$$\mathcal{L}_{plane} = \sum_{u,v \in \mathbb{P} \cap \mathbb{L}} \|\mathbf{M}_p[:, u, v] - \mathbf{M}_l[:, u, v]\|_2.$$

We use \mathcal{L}_{plane} to supervise the update of the constructed 3D plane, allowing it to approach the real ground and obtain accurate 3D ground positional information. An illustration demonstrating the efficacy of the proposed \mathcal{L}_{plane} is shown in Fig. 3.

3.4. Decoder

We build our decoder with L decoder layers following standard Transformer-based methods [2, 55]. In each layer, we use the query to predict 3D lane locations (x, y, z) as 3D reference points ref_{3D} and project each 3D point into the 2D image termed as ref_{2D} following Eq. (1). Then, we formulate the message exchange process using the lane-aware query embedding $\mathbf{Q} \in \mathbb{R}^{(N \times M) \times C}$ and the 3D ground positional embedding $\mathbf{PE} \in \mathbb{R}^{C \times (H \times W)}$ as follows:

$$\mathbf{Q}_l = \text{DeformAttn}(\mathbf{Q}_{l-1}, \mathbf{X}^\top + \mathbf{PE}^\top, \mathbf{X}^\top, ref_{2D}),$$

where $\mathbf{X} \in \mathbb{R}^{C \times (H \times W)}$ represents the extracted image feature map, l is the layer index, and DeformAttn is a standard deformable attention module [55]. As shown in Fig. 2, we also estimate the residual transformation matrix of our constructed plane as illustrated in Sec. 3.3 and iteratively adjust its locations similar to reference points. With this iterative refinement mechanism, LATR can progressively update its knowledge about 3D ground and improve its localizability.

3.5. Prediction Head and Losses

Prediction Head. We apply a prediction head on top of the query to generate our final predictions. For the 3D positions estimation, we use an MLP which can be formulated as:

$$[\Delta x, \Delta z, v] = \text{MLP}_{reg}(\mathbf{Q}),$$

where $\Delta x, \Delta z \in \mathbb{R}^{N \times M \times 1}$ represents the offsets *w.r.t.* the corresponding reference points (Sec. 3.4) in last decoder layer. And $v \in \mathbb{R}^{N \times M \times 1}$ denotes the visibility of each predicted lane point, which indicates whether the projected point is valid in the image. Together with the predefined longitudinal coordinate $\mathbf{Y}_{ref} \in \mathbb{R}^{M \times 1}$, we obtain N point sets as ref_{3D} . For the lane categories, we adopt max-pooling along the point dimension followed by a per-instance MLP:

$$\mathbf{C} = \text{MLP}_{cls}(\text{MaxPool}(\mathbf{Q})),$$

where $\mathbf{C} \in \mathbb{R}^{N \times K}$ denotes the class-logits and K is the number of possible classes. Lanes classified as “background” will be discarded in our final predictions. Here we apply the same bipartite matching results as our auxiliary segmentation in Sec. 3.2 for 3D lane label assignment. This strategy ensures consistent 2D segmentation and 3D lane detection supervision for each query.

Overall Loss. Given matched ground truth labels for the lane queries, we calculate the corresponding loss for each matched pair. Concretely, our total loss consists of three parts: the instance segmentation auxiliary loss \mathcal{L}_{seg} (Sec. 3.2), the 3D ground-aware plane update loss \mathcal{L}_{plane} (Sec. 3.3), and the 3D lane prediction loss \mathcal{L}_{lane} . Formally,

$$\begin{aligned} \mathcal{L}_{lane} &= w_x \mathcal{L}_x + w_z \mathcal{L}_z + w_v \mathcal{L}_v + w_c \mathcal{L}_c, \\ \mathcal{L} &= w_s \mathcal{L}_{seg} + w_p \mathcal{L}_{plane} + w_l \mathcal{L}_{lane}, \end{aligned}$$

where $w_{[*]}$ represent different loss weights: $w_s=5.0$,

Methods	F1 \uparrow	Category	X error (m) \downarrow		Z error (m) \downarrow	
		Accuracy \uparrow	<i>near</i>	<i>far</i>	<i>near</i>	<i>far</i>
3DLaneNet [7]	44.1	-	0.479	0.572	0.367	0.443
GenLaneNet [8]	32.3	-	0.593	0.494	0.140	0.195
Cond-IPM	36.6	-	0.563	1.080	0.421	0.892
Persformer* [3]	<u>50.5</u>	<u>89.5</u>	<u>0.319</u>	<u>0.325</u>	<u>0.112</u>	<u>0.141</u>
CurveFormer [1]	<u>50.5</u>	-	0.340	0.772	0.207	0.651
Persformer-Res50 \dagger	53.0	89.2	0.321	0.303	0.085	0.118
LATR-Lite	61.5	91.9	0.225	0.249	0.073	0.106
LATR	61.9 \uparrow 11.4	92.0 \uparrow 2.5	0.219 \downarrow 0.100	0.259 \downarrow 0.066	0.075 \downarrow 0.037	0.104 \downarrow 0.037

Table 1. **Comparison with other 3D lane detection methods on the OpenLane validation dataset.** * denotes the official released results. \dagger denotes the results reproduced by Persformer with ResNet50 and input image with shape of 720×960 for a fair comparison. \downarrow in the head row illustrates that the lower the metric value is, the better the performance is, and vice versa. Bold ones denote the best results and underline denotes the previous best results. The performance gains are demonstrated with blue arrows.

$w_x=2.0$, $w_z=10.0$, $w_c=10.0$, and the rest are set to 1.0. We use L1 loss for \mathcal{L}_x , \mathcal{L}_z and use BCE loss for \mathcal{L}_v . For classification, we adopt focal loss [19] with $\gamma=2.0$ and $\alpha=0.25$, same as [17, 25].

4. Experiments

We evaluate our method on three 3D lane benchmarks, OpenLane [3], Apollo [8] and ONCE-3DLanes [47].

4.1. Datasets and Metrics

OpenLane [3] is a large-scale benchmark for 3D lane detection, built on the Waymo dataset [39]. The dataset consists of 1000 segments, including 200K frames captured under various weather, terrain, and brightness conditions at a resolution of 1280×1920 . OpenLane contains 880K lane annotations distributed among 14 categories, providing a realistic and diverse set of challenges for 3D lane detection algorithms.

Apollo Synthetic [8] is generated using a game engine. It comprises over 10k images covering three distinct scenes: 1) *Balanced scenes*, 2) *Rarely observed scenes*, and 3) *Scenes with visual variations*. The dataset includes diversified terrain structures such as highways, urban, and residential areas, as well as various illumination conditions.

ONCE-3DLanes [47] is a real-world 3D lane dataset, built on the ONCE [31] dataset, which contains 211K images covering different regions, weather and lighting conditions.

Evaluation Metrics. We follow official evaluation metrics to investigate our model on the above two datasets. The evaluation is formulated as a matching problem based on minimum-cost flow, where the lane matching cost is obtained by taking the square root of the squared sum of point-wise distances over predefined ys . A lane prediction is considered matched if at least 75% of its points have a point-wise distance less than a predefined threshold of 1.5 meters [8, 3]. Errors are measured in the near range [0, 40]m and far range [40, 100]m along the heading direction. Moreover, the Average Precision (AP) metric is used to evaluate the performance on the Apollo Synthetic dataset [8].

4.2. Experimental Settings

Implementation Details. We use an input shape of 720×960 and adopt ResNet-50 [9] as our backbone to extract feature maps from three scales with spatial reduction ratios of $[\frac{1}{8}, \frac{1}{16}, \frac{1}{32}]$. After that, we exploit FPN [18] to generate multi-scale features, constructing a four-layer feature pyramid. Specifically, we apply dilation convolutions to upsample small feature maps into the largest scale, *i.e.*, the $\frac{1}{8}$ ratio, and aggregate all features as the input of our decoder. For the decoder, we employ deformable attention [55] with 4 attention heads, 8 sample points, and 256-D embeddings. Following the common setting of object detection [50], we use a 6-layer decoder in LATR as our default version and 2 layers as our lite version.

Training. All our experiments are trained with the AdamW optimizer with a weight decay of 0.01. We set the learning rate to be 2×10^{-4} and use a cosine annealing scheduler. We use batch size 32 and trained models on A100 GPUs. We train the models for 24 epochs on OpenLane and ONCE-3DLanes, and 100 epochs on Apollo datasets.

4.3. Main Results

Results on the OpenLane. We present the main results on OpenLane *val* set in Tab. 1. Several key trends can be observed: **1)** LATR surpasses all previous methods by substantial margins. It achieves a remarkable improvement of 11.4 in F1 score and 2.5 in category accuracy compared to the previous state-of-the-art method, Persformer [3]. **2)** LATR achieves significant reductions in both X and Z direction errors across both the near and far range, compared to the previous SOTA. Notably, the errors are reduced by 0.100m/0.066m and by 0.037m/0.037m in X and Z directions within the near/far range, respectively. **3)** LATR-Lite, albeit a lightweight version of LATR with only two decoder layers, attains comparable results to LATR. **4)** Although Persformer (Persformer-Res50) shows an increase in F1 from 50.5 to 53.0 by utilizing the same backbone and input shape as LATR, it still significantly lags behind LATR in performance. In Fig 4, we present the qualitative compar-

Scene	Methods	F1 \uparrow	AP \uparrow	X error (m) \downarrow		Z error (m) \downarrow	
				<i>near</i>	<i>far</i>	<i>near</i>	<i>far</i>
Balanced Scene	3DLaneNet [7]	86.4	89.3	0.068	0.477	0.015	0.202
	Gen-LaneNet [8]	88.1	90.1	0.061	0.496	0.012	0.214
	CLGo [21]	91.9	94.2	0.061	0.361	0.029	0.250
	PersFormer [3]	92.9	-	0.054	0.356	0.010	0.234
	GP [14]	91.9	93.8	<u>0.049</u>	0.387	<u>0.008</u>	<u>0.213</u>
	CurveFormer [1]	95.8	97.3	0.078	0.326	0.018	0.219
	LATR-Lite	96.5	97.8	0.035	0.283	0.012	0.209
	LATR	96.8 $\uparrow 1.0$	97.9 $\uparrow 0.6$	0.022 $\downarrow 0.027$	0.253 $\downarrow 0.073$	0.007 $\downarrow 0.001$	0.202 $\downarrow 0.011$
Rare Subset	3DLaneNet [7]	74.6	72.0	0.166	0.855	0.039	0.521
	Gen-LaneNet [8]	78.0	79.0	0.139	0.903	0.030	0.539
	CLGo [21]	86.1	88.3	0.147	0.735	0.071	0.609
	PersFormer [3]	87.5	-	<u>0.107</u>	0.782	0.024	0.602
	GP [14]	83.7	85.2	0.126	0.903	<u>0.023</u>	0.625
	CurveFormer [1]	95.6	97.1	0.182	0.737	0.039	0.561
	LATR-Lite	95.8	97.2	0.060	0.618	0.020	0.538
	LATR	96.1 $\uparrow 0.5$	97.3 $\uparrow 0.2$	0.050 $\downarrow 0.057$	0.600 $\downarrow 0.135$	0.015 $\downarrow 0.008$	0.532 $\uparrow 0.011$
Visual Variations	3DLaneNet [7]	74.9	72.5	0.115	0.601	0.032	0.230
	Gen-LaneNet [8]	85.3	87.2	0.074	0.538	0.015	0.232
	CLGo [21]	87.3	89.2	0.084	0.464	0.045	0.312
	PersFormer [3]	89.6	-	0.074	0.430	0.015	0.266
	GP [14]	89.9	92.1	<u>0.060</u>	0.446	0.011	0.235
	CurveFormer [1]	<u>90.8</u>	<u>93.0</u>	0.125	<u>0.410</u>	0.028	0.254
	LATR-Lite	94.0	95.6	0.048	0.352	0.018	0.231
	LATR	95.1 $\uparrow 4.3$	96.6 $\uparrow 3.6$	0.045 $\downarrow 0.015$	0.315 $\downarrow 0.095$	<u>0.016</u> $\uparrow 0.005$	0.228 $\downarrow 0.002$

Table 2. **Comparison with other 3D lane detection methods on Apollo 3D Synthetic dataset with three different scenes.** LATR achieves the best performance over all metrics and across three scenes with notable margins. Moreover, we implement a lite version, dubbed LATR-Lite, which consists of two decoder layers and achieves comparable results as LATR. Blue arrows denote gains, while red ones denote deterioration.

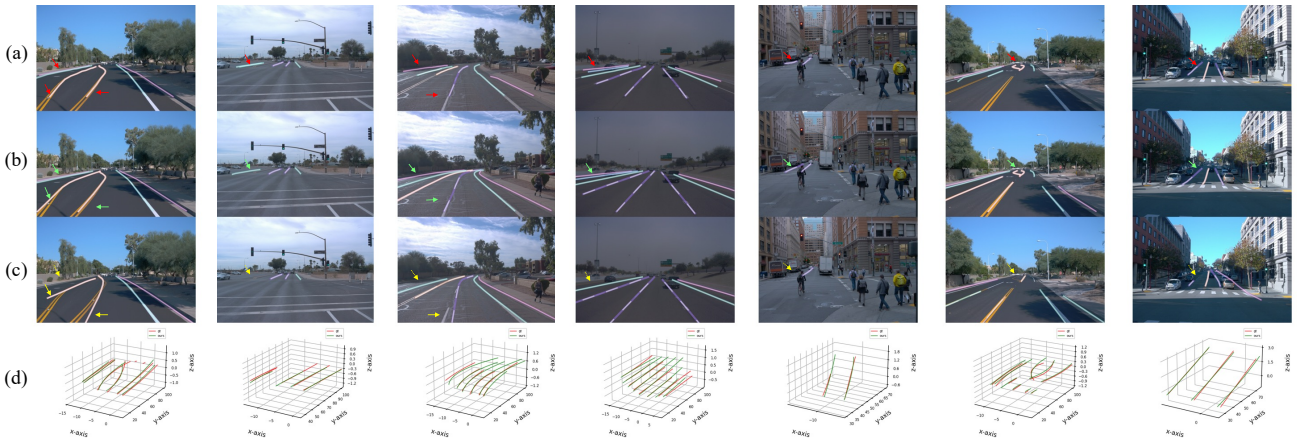


Figure 4. **Qualitative evaluation on OpenLane val set.** The rows (a), (b), (c) illustrate ground truth 3D lanes, prediction from LATR and Persformer [3] with 2D projection, respectively. Here, different colors indicate specific categories. Row (d) demonstrates the ground truth (red) and prediction of LATR (green) in 3D space. Best viewed in color (zoom in for details.)

comparison of LATR and Persformer [3], where our method performs more accurate predictions in several challenging scenarios. Besides, comprehensive studies of LATR under various scenarios are included in our Supplementary.

Results on the Apollo. Tab. 2 summarizes the results of our experiments on the Apollo dataset. We evaluate our method on three different scenes and study the F1 score, AP, and errors, following the literature [8]. Our LATR demonstrates superiority over all scenes and metrics, despite the performance being close to saturation. Notably, our design sig-

nificantly boosts the performance by 4.3 points in F1 and 3.6 points in AP under the visual variations scenario, which suggests the effectiveness of our dynamic ground design. Moreover, we observe that our model achieves comparable results with both 2-layer and 6-layer decoders.

Results on the ONCE-3DLanes exhibit similar trends to those on the OpenLane dataset and are included in the Supplementary, due to space limitations. These experiments on both realistic and synthetic datasets demonstrate the generalization and robustness of our proposed method, indicating

its potential to be applied in real-world scenarios.

4.4. Model Analysis

We conduct a thorough analysis to verify the efficacy of our design choice in LATR using the OpenLane-300 dataset [3], following the literature [3]. Additional details concerning model complexity and ablation studies (decoder layers, input size) are provided in our Supplementary.

Module Ablations. The first and third rows in Tab. 3 show the results of using learnable weights to replace the lane-level embedding. Using the learnable embedding, without prior knowledge of image features, performs much worse than its lane-aware counterpart (61.5 vs. 70.4 and 45.5 vs. 67.9 in F1 score). Furthermore, no matter how the lane-level embedding is obtained, noticeable performance drops are observed when the dynamic 3D ground PE is dropped from LATR. The gap becomes even more significant when learnable weights replace the lane-level embedding (61.5→45.5). Overall, when singly applied, each component in Tab. 3 significantly improves the performance over the baseline. Employing both designs further boost performance and achieved the best results.

Lane Embed	Ground Embed	F1 / C.Acc.	X error (m) <i>near</i> <i>far</i>	Z error (m) <i>near</i> <i>far</i>
		45.5 / 78.6	0.644 0.491	0.109 0.147
✓		67.9 / 90.3	0.281 0.349	0.102 0.139
	✓	61.5 / 87.7	0.352 0.381	0.101 0.140
✓	✓	70.4 / 92.9	0.241 0.321	0.097 0.132

Table 3. **Ablation studies on designed modules.** “Lane Embed” and “Ground Embed” denote lane-level embedding in Lane-aware Query Generator and Dynamic 3D ground PE Generator, respectively. *C.Acc.* means category accuracy.

Point-level Query vs. Lane-level Query. In LATR, each query is enhanced with the point-level embedding, corresponding to a single point in the final lane prediction. Every group of M points that belong to the same lane-level embedding is grouped together to form a complete lane. In this part, we explore another choice, using lane-level embedding $Q_{lane} \in \mathbb{R}^{N \times C}$ as the final query embeddings. Unlike the point-level query approach, this setup requires predicting M different points for each lane query. As shown in Tab. 4, using pure lane-level queries incurs a noticeable performance drop (*e.g.*, 70.4→66.5 in terms of F1) when compared to our proposed setup.

Effect of Dynamic 3D Ground Positional Embedding. To evaluate the effectiveness of our dynamic 3D ground positional embedding, we compared it with several alternatives. Specifically, we experimented with assigning 3D positions to image pixels using a fixed frustum [25] or a fixed ground plane, in addition to our proposed setup that leverages an iteratively updated ground plane. As shown in Tab. 5, adding 3D positional information to image pixels improves the per-

Model	F1 / C.Acc.	X error (m)		Z error (m)	
		<i>near</i>	<i>far</i>	<i>near</i>	<i>far</i>
Lane only	66.5 / 91.3	0.278	0.337	0.100	0.138
Lane + Point	70.4 / 92.9	0.241	0.321	0.097	0.132

Table 4. Different design choices for lane-aware queries.

formance regardless of the methods we use. As expected, we observed that generating 3D positions using a frustum shows inferior results compared to using a plane. This is reasonable given that lanes exist on the ground, and using a frustum will introduce a significant portion of points in the air where lanes are absent. Furthermore, Tab. 5 shows that using a dynamically updated plane is better than using a fixed one, demonstrating the effectiveness of our design choice.

Methods	F1 / C.Acc.	X error (m)		Z error (m)	
		<i>near</i>	<i>far</i>	<i>near</i>	<i>far</i>
-	67.9 / 90.3	0.281	0.349	0.102	0.139
Fixed Frustum	69.1 / 91.3	0.277	0.343	0.101	0.137
Fixed Plane	69.2 / 91.7	0.263	0.321	0.100	0.133
Dynamic Plane	70.4 / 92.9	0.241	0.321	0.097	0.132

Table 5. **Effect of dynamic 3D ground PE.** We compare the results of different 3D positional embedding designs.

5. Discussion

While our model significantly improves performance on three public datasets, even surpasses the multi-modal method [30], it does encounter some failure cases. As a vision-centric method, LATR is susceptible to the loss of visual cues (*e.g.*, glare or blur, invisible lanes in darkness, or severe shadows). These limitations can be observed in Supplementary Tab. 1. Incorporating inherent rich 3D geometric information in LiDAR may offer support in such challenging situations and potentially provide a more robust solution for 3D lane detection. The exploration of a multi-modal method is an open and intriguing avenue for future research.

6. Conclusion

In this work, we propose LATR, a simple yet effective end-to-end framework for 3D lane detection that achieves the best performance. It skips the surrogate view transformation and directly performs 3D lane detection on front-view features. We propose an effective lane-aware query generator to offer query informative priors and design a hybrid embedding to enhance query perception capability by aggregating lane-level and point-level features. Moreover, to build the 2D-3D connection, we devise a hypothetical 3D ground to encode 3D space information into 2D features. Extensive experiments show that LATR achieves remarkable performance. We believe that our work can benefit the community and inspire further research.

7. Acknowledge

This work was supported in part by Shenzhen General Program No.JCYJ20220530143600001, by the Basic Research Project No.HZQB-KCZYZ-2021067 of Hetao Shenzhen HK S&T Cooperation Zone, by Shenzhen-Hong Kong Joint Funding No.SGDX20211123112401002, by Shenzhen Outstanding Talents Training Fund, by Guangdong Research Project No.2017ZT07X152 and No.2019CX01X104, by the Guangdong Provincial Key Laboratory of Future Networks of Intelligence (Grant No.2022B1212010001), by the Guangdong Provincial Key Laboratory of Big Data Computing, The Chinese University of Hong Kong, Shenzhen, by the NSFC 61931024&81922046, by zelixir biotechnology company Fund, by Tencent Open Fund.

References

- [1] Yifeng Bai, Zhirong Chen, Zhangjie Fu, Lang Peng, Pengpeng Liang, and Erkang Cheng. Curveformer: 3d lane detection by curve propagation with curve queries and attention. *arXiv preprint arXiv:2209.07989*, 2022. [1](#), [2](#), [4](#), [6](#), [7](#)
- [2] Nicolas Carion, Francisco Massa, Gabriel Synnaeve, Nicolas Usunier, Alexander Kirillov, and Sergey Zagoruyko. End-to-end object detection with transformers. In *Computer Vision–ECCV 2020: 16th European Conference, Glasgow, UK, August 23–28, 2020, Proceedings, Part I 16*, pages 213–229. Springer, 2020. [2](#), [3](#), [4](#), [5](#)
- [3] Li Chen, Chonghao Sima, Yang Li, Zehan Zheng, Jiajie Xu, Xiangwei Geng, Hongyang Li, Conghui He, Jianping Shi, Yu Qiao, and Junchi Yan. Persformer: 3d lane detection via perspective transformer and the openlane benchmark. In *European Conference on Computer Vision (ECCV)*, 2022. [1](#), [2](#), [3](#), [4](#), [6](#), [7](#), [8](#)
- [4] Tianheng Cheng, Xinggang Wang, Shaoyu Chen, Wenqiang Zhang, Qian Zhang, Chang Huang, Zhaoxiang Zhang, and Wenyu Liu. Sparse instance activation for real-time instance segmentation. In *Proceedings of the IEEE/CVF Conference on Computer Vision and Pattern Recognition*, pages 4433–4442, 2022. [4](#)
- [5] Netalee Efrat, Max Bluvstein, Shaul Oron, Dan Levi, Noa Garnett, and Bat El Shlomo. 3d-lanenet+: Anchor free lane detection using a semi-local representation. *arXiv preprint arXiv:2011.01535*, 2020. [1](#), [2](#), [4](#)
- [6] Zhengyang Feng, Shaohua Guo, Xin Tan, Ke Xu, Min Wang, and Lizhuang Ma. Rethinking efficient lane detection via curve modeling. In *Proceedings of the IEEE/CVF Conference on Computer Vision and Pattern Recognition*, pages 17062–17070, 2022. [2](#)
- [7] Noa Garnett, Rafi Cohen, Tomer Pe’er, Roei Lahav, and Dan Levi. 3d-lanenet: end-to-end 3d multiple lane detection. In *Proceedings of the IEEE/CVF International Conference on Computer Vision*, pages 2921–2930, 2019. [1](#), [2](#), [3](#), [4](#), [6](#), [7](#)
- [8] Yuliang Guo, Guang Chen, Peitao Zhao, Weide Zhang, Jinghao Miao, Jingao Wang, and Tae Eun Choe. Gen-lanenet: A generalized and scalable approach for 3d lane detection. In *European Conference on Computer Vision*, pages 666–681. Springer, 2020. [1](#), [2](#), [3](#), [4](#), [6](#), [7](#)
- [9] Kaiming He, Xiangyu Zhang, Shaoqing Ren, and Jian Sun. Deep residual learning for image recognition. In *Proceedings of the IEEE conference on computer vision and pattern recognition*, pages 770–778, 2016. [6](#)
- [10] Kuan-Chih Huang, Tsung-Han Wu, Hung-Ting Su, and Winston H Hsu. Monodtr: Monocular 3d object detection with depth-aware transformer. In *Proceedings of the IEEE/CVF Conference on Computer Vision and Pattern Recognition*, pages 4012–4021, 2022. [3](#)
- [11] Dongkwon Jin, Wonhui Park, Seong-Gyun Jeong, Heeyeon Kwon, and Chang-Su Kim. Eigenlanes: Data-driven lane descriptors for structurally diverse lanes. In *Proceedings of the IEEE/CVF Conference on Computer Vision and Pattern Recognition*, pages 17163–17171, 2022. [2](#)
- [12] Yeongmin Ko, Younkwan Lee, Shoab Azam, Farzeen Munir, Moongu Jeon, and Witold Pedrycz. Key points estimation and point instance segmentation approach for lane detection. *IEEE Transactions on Intelligent Transportation Systems*, 23(7):8949–8958, 2021. [2](#)
- [13] Alex H Lang, Sourabh Vora, Holger Caesar, Lubing Zhou, Jiong Yang, and Oscar Beijbom. Pointpillars: Fast encoders for object detection from point clouds. In *Proceedings of the IEEE/CVF conference on computer vision and pattern recognition*, pages 12697–12705, 2019. [1](#)
- [14] Chenguang Li, Jia Shi, Ya Wang, and Guangliang Cheng. Reconstruct from top view: A 3d lane detection approach based on geometry structure prior. In *Proceedings of the IEEE/CVF Conference on Computer Vision and Pattern Recognition*, pages 4370–4379, 2022. [1](#), [2](#), [3](#), [4](#), [7](#)
- [15] Xiang Li, Jun Li, Xiaolin Hu, and Jian Yang. Line-cnn: End-to-end traffic line detection with line proposal unit. *IEEE Transactions on Intelligent Transportation Systems*, 21(1):248–258, 2019. [2](#)
- [16] Yinhao Li, Zheng Ge, Guanyi Yu, Jinrong Yang, Zengran Wang, Yukang Shi, Jianjian Sun, and Zeming Li. Bevdepth: Acquisition of reliable depth for multi-view 3d object detection. *arXiv preprint arXiv:2206.10092*, 2022. [3](#)
- [17] Zhiqi Li, Wenhai Wang, Hongyang Li, Enze Xie, Chonghao Sima, Tong Lu, Yu Qiao, and Jifeng Dai. Bevformer: Learning bird’s-eye-view representation from multi-camera images via spatiotemporal transformers. In *Computer Vision–ECCV 2022: 17th European Conference, Tel Aviv, Israel, October 23–27, 2022, Proceedings, Part IX*, pages 1–18. Springer, 2022. [3](#), [4](#), [6](#)
- [18] Tsung-Yi Lin, Piotr Dollár, Ross Girshick, Kaiming He, Bharath Hariharan, and Serge Belongie. Feature pyramid networks for object detection. In *Proceedings of the IEEE conference on computer vision and pattern recognition*, pages 2117–2125, 2017. [6](#)
- [19] Tsung-Yi Lin, Priya Goyal, Ross Girshick, Kaiming He, and Piotr Dollár. Focal loss for dense object detection. In *Proceedings of the IEEE international conference on computer vision*, pages 2980–2988, 2017. [6](#)
- [20] Lizhe Liu, Xiaohao Chen, Siyu Zhu, and Ping Tan. Condlanenet: a top-to-down lane detection framework based on

- conditional convolution. In *Proceedings of the IEEE/CVF international conference on computer vision*, pages 3773–3782, 2021. 2
- [21] Ruijin Liu, Dapeng Chen, Tie Liu, Zhiliang Xiong, and Zejian Yuan. Learning to predict 3d lane shape and camera pose from a single image via geometry constraints. In *Proceedings of the AAAI Conference on Artificial Intelligence*, volume 36, pages 1765–1772, 2022. 7
- [22] Rosanne Liu, Joel Lehman, Piero Molino, Felipe Petroski Such, Eric Frank, Alex Sergeev, and Jason Yosinski. An intriguing failing of convolutional neural networks and the coordconv solution. *Advances in neural information processing systems*, 31, 2018. 4
- [23] Ruijin Liu, Zejian Yuan, Tie Liu, and Zhiliang Xiong. End-to-end lane shape prediction with transformers. In *Proceedings of the IEEE/CVF winter conference on applications of computer vision*, pages 3694–3702, 2021. 1, 2
- [24] Shilong Liu, Feng Li, Hao Zhang, Xiao Yang, Xianbiao Qi, Hang Su, Jun Zhu, and Lei Zhang. Dab-detr: Dynamic anchor boxes are better queries for detr. *arXiv preprint arXiv:2201.12329*, 2022. 3
- [25] Yingfei Liu, Tiancai Wang, Xiangyu Zhang, and Jian Sun. Petr: Position embedding transformation for multi-view 3d object detection. In *Computer Vision–ECCV 2022: 17th European Conference, Tel Aviv, Israel, October 23–27, 2022, Proceedings, Part XXVII*, pages 531–548. Springer, 2022. 3, 4, 6, 8
- [26] Yingfei Liu, Junjie Yan, Fan Jia, Shuailin Li, Qi Gao, Tiancai Wang, Xiangyu Zhang, and Jian Sun. Petrv2: A unified framework for 3d perception from multi-camera images. *arXiv preprint arXiv:2206.01256*, 2022. 3
- [27] Yuxuan Liu, Yuan Yixuan, and Ming Liu. Ground-aware monocular 3d object detection for autonomous driving. *IEEE Robotics and Automation Letters*, 6(2):919–926, 2021. 4
- [28] Zhijian Liu, Haotian Tang, Alexander Amini, Xinyu Yang, Huihui Mao, Daniela Rus, and Song Han. Bevfusion: Multi-task multi-sensor fusion with unified bird’s-eye view representation. *arXiv preprint arXiv:2205.13542*, 2022. 3
- [29] Yan Lu, Xinzhu Ma, Lei Yang, Tianzhu Zhang, Yating Liu, Qi Chu, Junjie Yan, and Wanli Ouyang. Geometry uncertainty projection network for monocular 3d object detection. In *Proceedings of the IEEE/CVF International Conference on Computer Vision*, pages 3111–3121, 2021. 3
- [30] Yueru Luo, Xu Yan, Chaoda Zheng, Chao Zheng, Shuqi Mei, Tang Kun, Shuguang Cui, and Zhen Li. M⁺ 2-3d-lanenet: Multi-modal 3d lane detection. *arXiv preprint arXiv:2209.05996*, 2022. 2, 8
- [31] Jiageng Mao, Minzhe Niu, Chenhan Jiang, Xiaodan Liang, Yamin Li, Chaoqiang Ye, Wei Zhang, Zhenguo Li, Jie Yu, Chunjing Xu, et al. One million scenes for autonomous driving: Once dataset. 2021. 6
- [32] Davy Neven, Bert De Brabandere, Stamatios Georgoulis, Marc Proesmans, and Luc Van Gool. Towards end-to-end lane detection: an instance segmentation approach. In *2018 IEEE intelligent vehicles symposium (IV)*, pages 286–291. IEEE, 2018. 2
- [33] X Pan, J Shi, P Luo, X Wang, and X Tang. Spatial as deep: spatial cnn for traffic scene understanding. 2017. *Pan X Shi J Luo P Spatial As Deep: Spatial CNN for Traffic Scene Understanding*, 10, 2017. 2
- [34] Zequn Qin and Xi Li. Monoground: Detecting monocular 3d objects from the ground. In *Proceedings of the IEEE/CVF Conference on Computer Vision and Pattern Recognition*, pages 3793–3802, 2022. 3, 4
- [35] Zequn Qin, Huanyu Wang, and Xi Li. Ultra fast structure-aware deep lane detection. In *Computer Vision–ECCV 2020: 16th European Conference, Glasgow, UK, August 23–28, 2020, Proceedings, Part XXIV 16*, pages 276–291. Springer, 2020. 2
- [36] Zequn Qin, Pengyi Zhang, and Xi Li. Ultra fast deep lane detection with hybrid anchor driven ordinal classification. *IEEE Transactions on Pattern Analysis and Machine Intelligence*, 2022. 2
- [37] Zhan Qu, Huan Jin, Yang Zhou, Zhen Yang, and Wei Zhang. Focus on local: Detecting lane marker from bottom up via key point. In *Proceedings of the IEEE/CVF Conference on Computer Vision and Pattern Recognition*, pages 14122–14130, 2021. 2
- [38] Cody Reading, Ali Harakeh, Julia Chae, and Steven L Waslander. Categorical depth distribution network for monocular 3d object detection. In *Proceedings of the IEEE/CVF Conference on Computer Vision and Pattern Recognition*, pages 8555–8564, 2021. 4
- [39] Pei Sun, Henrik Kretzschmar, Xerxes Dotiwalla, Aurelien Chouard, Vijaysai Patnaik, Paul Tsui, James Guo, Yin Zhou, Yuning Chai, Benjamin Caine, et al. Scalability in perception for autonomous driving: Waymo open dataset. In *Proceedings of the IEEE/CVF conference on computer vision and pattern recognition*, pages 2446–2454, 2020. 6
- [40] Zhiqing Sun, Shengcao Cao, Yiming Yang, and Kris M Kitani. Rethinking transformer-based set prediction for object detection. In *Proceedings of the IEEE/CVF international conference on computer vision*, pages 3611–3620, 2021. 3
- [41] Lucas Tabelini, Rodrigo Berriel, Thiago M Paixao, Claudine Badue, Alberto F De Souza, and Thiago Oliveira-Santos. Keep your eyes on the lane: Real-time attention-guided lane detection. In *Proceedings of the IEEE/CVF conference on computer vision and pattern recognition*, pages 294–302, 2021. 2
- [42] Lucas Tabelini, Rodrigo Berriel, Thiago M Paixao, Claudine Badue, Alberto F De Souza, and Thiago Oliveira-Santos. Poly-lanenet: Lane estimation via deep polynomial regression. In *2020 25th International Conference on Pattern Recognition (ICPR)*, pages 6150–6156. IEEE, 2021. 2
- [43] Jinsheng Wang, Yinchao Ma, Shaofei Huang, Tianrui Hui, Fei Wang, Chen Qian, and Tianzhu Zhang. A keypoint-based global association network for lane detection. In *Proceedings of the IEEE/CVF Conference on Computer Vision and Pattern Recognition*, pages 1392–1401, 2022. 2
- [44] Yan Wang, Wei-Lun Chao, Divyansh Garg, Bharath Hariharan, Mark Campbell, and Kilian Q Weinberger. Pseudo-lidar from visual depth estimation: Bridging the gap in 3d object detection for autonomous driving. In *Proceedings of the IEEE/CVF Conference on Computer Vision and Pattern Recognition*, pages 8445–8453, 2019. 4

- [45] Yingming Wang, Xiangyu Zhang, Tong Yang, and Jian Sun. Anchor detr: Query design for transformer-based object detection. *arXiv preprint arXiv:2109.07107*, 3(6), 2021. [3](#)
- [46] Kyle R Williams, Rachel Schlossman, Daniel Whitten, Joe Ingram, Srideep Musuvathy, James Pagan, Kyle A Williams, Sam Green, Anirudh Patel, Anirban Mazumdar, et al. Trajectory planning with deep reinforcement learning in high-level action spaces. *IEEE Transactions on Aerospace and Electronic Systems*, 2022. [1](#)
- [47] Fan Yan, Ming Nie, Xinyue Cai, Jianhua Han, Hang Xu, Zhen Yang, Chaoqiang Ye, Yanwei Fu, Michael Bi Mi, and Li Zhang. Once-3dlanes: Building monocular 3d lane detection. In *Proceedings of the IEEE/CVF Conference on Computer Vision and Pattern Recognition*, pages 17143–17152, 2022. [1](#), [2](#), [6](#)
- [48] Fan Yang, Xinhao Xu, Hui Chen, Yuchen Guo, Jungong Han, Kai Ni, and Guiguang Ding. Ground plane matters: Picking up ground plane prior in monocular 3d object detection. *arXiv preprint arXiv:2211.01556*, 2022. [4](#)
- [49] Seungwoo Yoo, Hee Seok Lee, Heesoo Myeong, Sungrack Yun, Hyoungwoo Park, Janghoon Cho, and Duck Hoon Kim. End-to-end lane marker detection via row-wise classification. In *Proceedings of the IEEE/CVF Conference on Computer Vision and Pattern Recognition Workshops*, pages 1006–1007, 2020. [2](#)
- [50] Renrui Zhang, Han Qiu, Tai Wang, Ziyu Guo, Ziteng Cui, Yu Qiao, Hao Dong, Peng Gao, and Hongsheng Li. Monodetr: Depth-guided transformer for monocular 3d object detection. [3](#), [6](#)
- [51] Renrui Zhang, Han Qiu, Tai Wang, Xuanzhuo Xu, Ziyu Guo, Yu Qiao, Peng Gao, and Hongsheng Li. Monodetr: Depth-aware transformer for monocular 3d object detection. *arXiv preprint arXiv:2203.13310*, 2022. [3](#)
- [52] Tu Zheng, Hao Fang, Yi Zhang, Wenjian Tang, Zheng Yang, Haifeng Liu, and Deng Cai. Resa: Recurrent feature-shift aggregator for lane detection. In *Proceedings of the AAAI Conference on Artificial Intelligence*, volume 35, pages 3547–3554, 2021. [2](#)
- [53] Tu Zheng, Yifei Huang, Yang Liu, Wenjian Tang, Zheng Yang, Deng Cai, and Xiaofei He. Clrnet: Cross layer refinement network for lane detection. In *Proceedings of the IEEE/CVF conference on computer vision and pattern recognition*, pages 898–907, 2022. [2](#)
- [54] Yin Zhou and Oncel Tuzel. Voxelnet: End-to-end learning for point cloud based 3d object detection. In *Proceedings of the IEEE conference on computer vision and pattern recognition*, pages 4490–4499, 2018. [1](#)
- [55] Xizhou Zhu, Weijie Su, Lewei Lu, Bin Li, Xiaogang Wang, and Jifeng Dai. Deformable detr: Deformable transformers for end-to-end object detection. *arXiv preprint arXiv:2010.04159*, 2020. [2](#), [3](#), [4](#), [5](#), [6](#)